Modelling of GNSS Positioning Errors in a GNSS/INS/LiDAR-integrated Georeferencing

Florian Pöppl[1], Martin Pfennigbauer[2], Andreas Ullrich[2], Gottfried Mandlburger[1], Hans Neuner[1] & Norbert Pfeifer[1]

Abstract: Kinematic laser scanning is an efficient and highly accurate method for the acquisition of 3D topographic data. A primary task in kinematic laser scanning is the transformation of the laser scanner measurements from a local scanner coordinate system to a global georeferenced coordinate system. This requires knowledge of the scanners' trajectory (position and orientation over time). The trajectory is typically computed via Kalman filtering of Global Navigation Satellite System (GNSS) and Inertial Navigation System (INS) measurement data. However, this trajectory often exhibits significant errors, which become apparent when point clouds acquired at different times overlap spatially. In these overlapping areas, corresponding points may be exploited in a subsequent strip adjustment to improve the trajectory and the system calibration and therefore the final point cloud. However, ignoring the raw GNSS and INS measurements and their statistical properties can lead to over-optimistic estimates and deformation of the laser point cloud. In this contribution, a method is presented which integrates the GNSS position, raw inertial measurements and laser scanner correspondences into one adjustment and explicitly models the time-correlated stochastic errors of the GNSS positioning solution. This method for direct georeferencing considerably reduces the discrepancies between overlapping point clouds, as demonstrated on an airborne laser scanning dataset in comparison with an existing state-of-the-art strip adjustment implementation.

1 Georeferencing for Kinematic Laser Scanning

Georeferencing is an important task in kinematic laser scanning, since most use-cases require the acquired point cloud to be in a suitable georeferenced coordinate system. The default way of achieving this involves GNSS (Global Navigation Satellite System), which provides absolute positioning, and INS (Inertial Navigation System), which provides high frequency relative position and orientation. Classically, GNSS and INS are fused via Kalman filtering to obtain the platform trajectory. When the geometric relation between platform and laser scanner is known, the laser measurements can be transformed from the scanner's coordinate system into the platforms' coordinate system and then into the earth-referenced coordinate system of the trajectory (Fig. 1). These errors in turn propagate through the georeferencing and result in errors in the point clouds, which become visible as discrepancies in areas that are scanned several times. This can be partially rectified by identifying correspondences in overlapping areas and introducing them as observations

[1] Technische Universität Wien, Department für Geodäsie und Geoinformation, Wiedner Hauptstraße 8, 1040 Wien, Österreich, E-Mail: [florian.poeppl, gottfried.mandlburger, hans.neuner, norbert.pfeifer]@geo.tuwien.ac.at
[2] RIEGL Laser Measurement Systems GmbH, Riedenburgstrasse 48, 3580 Horn, Austria, E-Mail: [mpfennigbauer, aullrich]@riegl.com

 DOI: 10.24407/KXP:1841080098

in a strip adjustment (Fig. 2, FILIN & VOSSELMAN 2004; KAGER 2004), thereby correcting errors in position and/or orientation and possibly the laser scanner calibration.

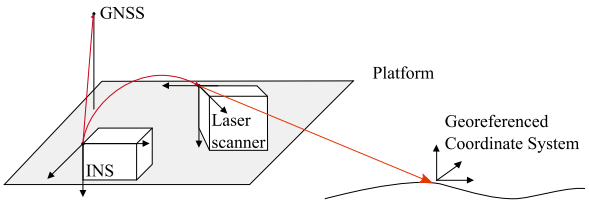

Fig. 1: GNSS antenna, INS and laser scanner mounted rigidly on the multi-sensor platform

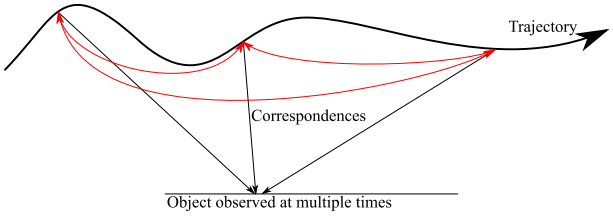

Fig. 2: Corresponding points on the ground form constraints on the trajectory at the acquisition times

However, such an approach is typically based on correcting the existing trajectory, and does not take into account the underlying GNSS or INS measurements or their stochastic properties. To allow correction of time-varying errors, a flexible trajectory correction model (e.g. splines) must be used, leading to an increase in the number of parameters. Without sufficient ground control this results in overparametrization and overfitting of the model as well as in systematic deformation of the point cloud (GLIRA et al. 2016).

In this work, a different approach is presented: The position observations from an initial GNSS-only processing are combined with the inertial measurements in a non-linear least-squares adjustment to produce an initial trajectory, which is used for a first georeferencing of the laser data. Then, correspondences are extracted from overlaps in the laser point cloud and used as input to a single least-squares adjustment together with the GNSS positions and inertial measurements. This allows simultaneous determination of time-constant calibration parameters, time-varying errors in the inertial sensors, and the trajectory (Tab. 1). Conceptually, this is a tight coupling of laser scanner measurements with the INS and a loose coupling with the GNSS, where information from the laser measurements helps to stabilize the INS drift. However, loose coupling of the GNSS poses its own challenges. The errors in the GNSS positioning may be correlated in time and in space due to a) the processing itself – usually via Kalman filter – and b) not fully modelled systematic errors such as ionospheric or tropospheric effects. Depending on the strength of the correlations, disregarding the time-correlated nature of the GNSS position observations leads to overly optimistic or biased parameter estimates. We propose explicitly accounting for the time-correlation in the stochastic model by assuming an additional stochastic error term modelled by a first-order Gauss-Markov process. This is similar to how inertial sensor errors are commonly modelled (FARRELL et al. 2022). Applying this to GNSS errors is not new in the context of Kalman filters (NIU et al. 2018), but has to our knowledge never been done in the context of batch least-squares estimation in general or strip adjustment in particular. We also present a simple yet effective way of estimating the relevant parameters of the stochastic model.

In Section 2, we will first discuss the methodology and then in Section 3 demonstrate our approach by applying it to an airborne laser scanning dataset. This dataset was acquired with a RIEGL VUX-160[23] laser scanner. The scanner features three differently oriented mirror facets, resulting in three *views*: nadir, +10 degrees forward, and -10 degrees backward (Fig. 3). A comparison of the strip

differences of a) strip adjustment with constant per-strip trajectory correction, b) our method with uncorrelated GNSS error model and c) our method with time-correlated GNSS error model shows significantly reduced discrepancies for our proposed approach (c).

Fig. 3: RIEGL VUX-16023 scan pattern with nadir/forward/backward views

2 Integrated Georeferencing with Time-Correlated GNSS Errors

2.1 GNSS/INS/LiDAR-Integrated Georeferencing

In this section, we describe the functional and stochastic models for the trajectory estimation using pre-processed GNSS positions, raw inertial measurements from the INS and correspondences extracted from the LiDAR point cloud. This approach employs batch non-linear least-squares estimation, where the discrepancies between the model predictions and a given set of measurements are minimized. The least-squares minimization is solved by non-linear optimization techniques, namely the Levenberg-Marquardt algorithm as implemented in the Ceres library (AGARWAL et al. 2022).

Figure 4 shows the processing pipeline for the GNSS/INS/LiDAR integration. The main steps are:

1. Computing an initial trajectory from GNSS/INS data via batch least-squares adjustment, using a Kalman filter to initialize trajectory parameters for the non-linear optimization.
2. Georeferencing of the LiDAR data with the initial trajectory and calibration parameters to obtain an initial point cloud for identifying correspondences.
3. Computing an improved trajectory and calibration with a batch least-squares adjustment of all available data: GNSS, INS and LiDAR.
4. Georeferencing of the LiDAR data with the improved trajectory and calibration to obtain the final point cloud.

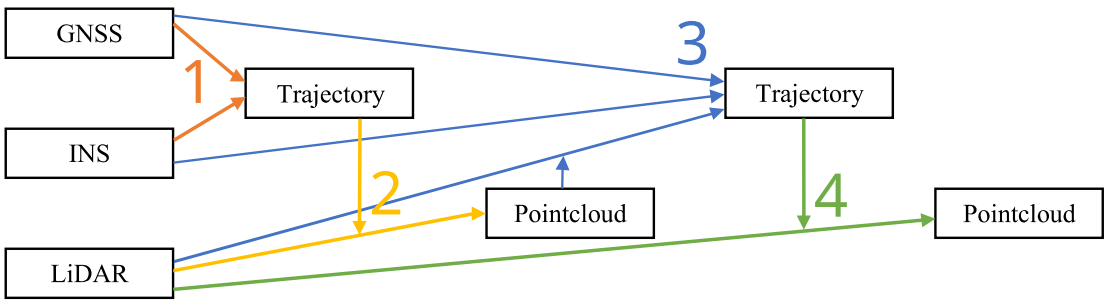

Fig. 4: Processing pipeline for GNSS/INS/LiDAR integration

The rest of this section describes the details of the least-squares adjustment in step 1 and step 3. A summary of the parameters occurring in the least-squares estimation is given in Tab. 1.

Tab. 1: Parameters for the least-squares estimation.

Trajectory	• Position: cubic spline with coefficients $\boldsymbol{x}_p \in \mathbb{R}^{3x(n+2)}$, provides a continuous position $\boldsymbol{p}(t, \boldsymbol{x}_p) \in \mathbb{R}^3$ of the platform in the local coordinate system. • Orientation: quadratic quaternion spline with coefficients $\boldsymbol{x}_o \in \mathbb{R}^{4x(n+1)}$, provides a continuous platform orientation $\mathbf{R}(t, \boldsymbol{x}_o) \in \mathrm{SO}(3)$, i.e., the rotation from the platform coordinate system to the local coordinate system. Position and orientation are with respect to a *local tangent plane coordinate system*. Spline nodes are set at the sample times of the n inertial measurements. To simplify presentation, we define the platform coordinate system to be identical to the INS coordinate system.
GNSS	• Antenna lever-arm $\boldsymbol{l}_a \in \mathbb{R}^3$: antenna position in platform coordinate system. • GNSS bias $\boldsymbol{b}_g \in \mathbb{R}^{3\mathrm{xm}}$: time-varying bias in xyz coordinates of the local coordinate system, modelled as a Gauss-Markov process. Bias parameters are estimated for all m GNSS measurement.
INS	• Accelerometer bias $\boldsymbol{b}_f \in \mathbb{R}^{3xm}$: time-varying random walk process. • Accelerometer scale-factor $\boldsymbol{s}_f \in \mathbb{R}^3$: time-constant. • Gyroscope bias $\boldsymbol{b}_\omega \in \mathbb{R}^{3xm}$: time-varying random walk process. • Gyroscope scale-factor $\boldsymbol{s}_\omega \in \mathbb{R}^3$: time-constant. Time-varying INS biases are estimated at the sample times of the m GNSS measurement and linearly interpolated in-between.
LiDAR	• Scanner boresight angles $\boldsymbol{\kappa} \in [0, 2\pi)^3$: defines the rotation $\mathbf{R}(\boldsymbol{\kappa})$ from the scanner coordinate system to the platform coordinate system. • Scanner lever-arm $\boldsymbol{l}_s \in \mathbb{R}^3$: scanner origin in the platform coordinate system.
Objects	• Plane offset and slope parameters $(o, z_1, z_2) \in \mathbb{R}^3$ per object plane.

Trajectory model: The trajectory is modelled as a continuous-time function. Standard cubic B-Splines are used for position and quadratic quaternion splines (KIM et al. 1995) for orientation. The continuous-time representation allows to evaluate the trajectory at any given time t. This is especially relevant for the high-frequency LiDAR data, where estimating the position and orientation for each emitted laser shot is unfeasible. In contrast to the spline-correction approach used in (GLIRA et al. 2016), the splines here are used to model the trajectory itself, with spline parameters introduced at the frequency of the inertial measurements. The aforementioned problem of overparametrization and block deformation is addressed by incorporating the raw inertial measurements and the GNSS position measurements in the strip adjustment, allowing for a highly flexible trajectory model without reducing redundancy.

GNSS measurement model: The GNSS is integrated in a loosely coupled manner. The raw measurements (pseudo-range, carrier-phase, Doppler) are first processed using a carrier-phase differential kinematic GNSS solution, in this case using the software package RTKLib (TAKASU & YASUDA 2009) in post-processing mode. The GNSS processing provides timestamped positions $\tilde{\boldsymbol{p}}$ and estimates of their precision. The predicted position of the GNSS antenna at time t can be derived directly from platform position $\boldsymbol{p}(t, \boldsymbol{x}_p)$, orientation $\mathbf{R}(t, \boldsymbol{x}_o)$ and GNSS lever arm $\boldsymbol{l}_a$. The measurement is assumed to be contaminated with an additive error $\boldsymbol{\epsilon}_p$. In total, the GNSS measurement equation for a measurement at time t is given by

$$\underbrace{\tilde{\boldsymbol{p}}}_{\text{measurement}} = \underbrace{\boldsymbol{p}(t, \boldsymbol{x}_p) + \mathbf{R}(t, \boldsymbol{x}_o)\boldsymbol{l}_a}_{\text{model}} + \underbrace{\boldsymbol{\epsilon}_p}_{\text{error}}. \tag{1}$$

Inertial measurement model: The measurements $\tilde{\boldsymbol{f}}, \tilde{\boldsymbol{\omega}}$ of the specific force $\boldsymbol{f}$ and angular rate $\boldsymbol{\omega}$ at time $\boldsymbol{t}$ include systematic errors (bias $\boldsymbol{b}_f/\boldsymbol{b}_\omega$ and scale factor $\boldsymbol{s}_f/\boldsymbol{s}_\omega$) and additive noise $\boldsymbol{\epsilon}_f/\boldsymbol{\epsilon}_\omega$

$$\begin{aligned} \tilde{\boldsymbol{f}} &= (\boldsymbol{I}_3 + \boldsymbol{S}_f)\boldsymbol{f} + \boldsymbol{b}_f + \boldsymbol{\epsilon}_f \\ \underbrace{\tilde{\boldsymbol{\omega}}}_{\text{measurement}} &= \underbrace{(\boldsymbol{I}_3 + \boldsymbol{S}_\omega)\boldsymbol{\omega} + \boldsymbol{b}_\omega}_{\text{model}} + \underbrace{\boldsymbol{\epsilon}_\omega}_{\text{error}}. \end{aligned} \tag{2}$$

Non-orthogonality is not considered, thus $\boldsymbol{S}_f = \mathrm{diag}(\boldsymbol{s}_f)$ and $\boldsymbol{S}_\omega = \mathrm{diag}(\boldsymbol{s}_\omega)$. The predicted specific force $\boldsymbol{f}$ and angular velocity $\boldsymbol{\omega}$ are computed via inertial navigation equations (GROVES 2013; PÖPPL et al. 2023) and depend on platform position $\boldsymbol{p}(t, \boldsymbol{x}_p)$ and orientation $\mathbf{R}(t, \boldsymbol{x}_o)$.

LiDAR measurement model: The LiDAR-derived measurements are based on detecting and matching planar features in the point clouds. Points from all strips are rasterized with cell size of $[h_x, h_y, h_z]$ and a best-fitting plane is computed via principal component analysis (PCA) of all points within each cell (Fig. 5 and Fig. 6). Raster cells are classified as valid based on certain planarity conditions, e.g., if the smallest eigenvalue is below a given threshold. From this, we derive the plane center $\tilde{\boldsymbol{c}}$ and (unit-length) normal $\tilde{\boldsymbol{n}}$. The plane center and normal are stored internally in the scanner coordinate system $(\tilde{\boldsymbol{c}}_s, \tilde{\boldsymbol{n}}_s)$ and transformed into the local coordinate system according to the georeferencing equations

$$\begin{aligned} \tilde{\boldsymbol{c}} &= \mathbf{R}(t, \boldsymbol{x}_o)\mathbf{R}(\boldsymbol{\kappa})(\tilde{\boldsymbol{c}}_s + \boldsymbol{l}_s) + \boldsymbol{p}(t, \boldsymbol{x}_p), \\ \tilde{\boldsymbol{n}} &= \mathbf{R}(t, \boldsymbol{x}_o)\mathbf{R}(\boldsymbol{\kappa})\tilde{\boldsymbol{n}}_s. \end{aligned} \tag{3}$$

Every such *feature plane* is assigned the time t of the closest actual LiDAR point. The feature planes serve as LiDAR measurements $(\tilde{\boldsymbol{c}}_s, \tilde{\boldsymbol{n}}_s)$ in the least-squares estimation. They are not actual measurements but rather each derived from multiple LiDAR points.

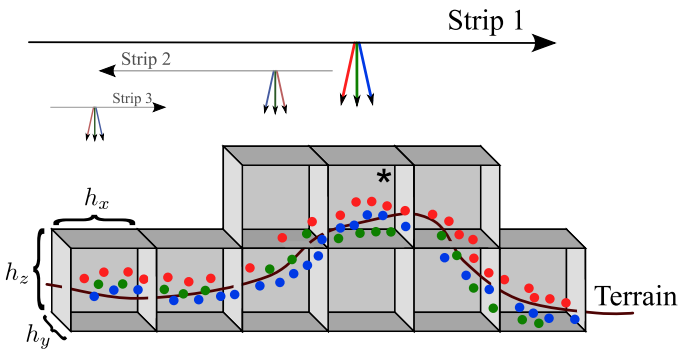

Fig. 5: All points are sorted into 3D raster cells but considered separately for each strip and view. Points are colored by view: forward (blue) / nadir (green) / backward (red)

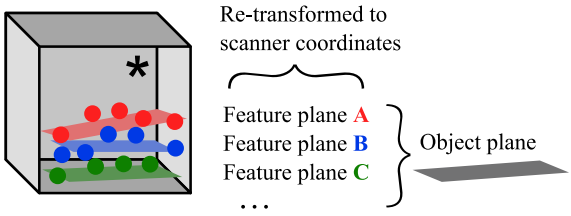

Fig. 6: For each strip and view, a feature plane is computed for the points in each raster cell via PCA. Feature planes in a cell are then associated with a corresponding object plane.

All feature planes in a given raster cell are aggregated into an *object plane*. This object plane corresponds to the actual physical plane, which is observed multiple times. Initially, each object plane is defined by a center $\boldsymbol{c^0}$ and (unit-length) normal $\boldsymbol{n}^0$, as well as (unit-length) axes $\boldsymbol{k}_1^0, \boldsymbol{k}_2^0$ so that $\boldsymbol{n}^0 = \boldsymbol{k}_1^0 \times \boldsymbol{k}_2^0$. For the least-squares adjustment, object planes are parametrized by an offset o and slopes z_1/z_2, with resulting center, axes and normal

$$\boldsymbol{c} \coloneqq \boldsymbol{c}_0 + o\,\boldsymbol{n}^0,\ \boldsymbol{k_1} \coloneqq \frac{\boldsymbol{k}_1^0+z_1\boldsymbol{n}^0}{\|\boldsymbol{k}_1^0+z_1\boldsymbol{n}^0\|},\ \boldsymbol{k_2} \coloneqq \frac{\boldsymbol{k}_2^0+z_2\boldsymbol{n}^0}{\|\boldsymbol{k}_2^0+z_2\boldsymbol{n}^0\|},\ \boldsymbol{n} \coloneqq \boldsymbol{k}_1 \times \boldsymbol{k}_2. \tag{4}$$

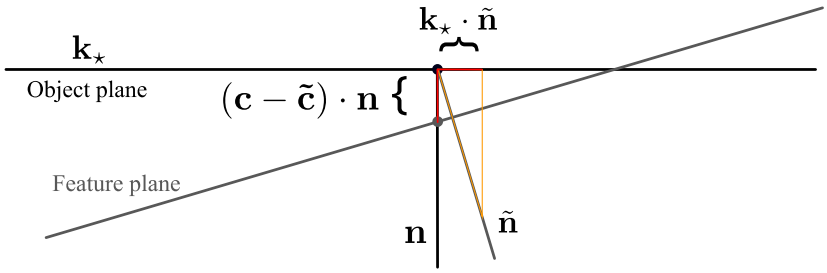

Fig. 7: Plane observation model: 1) Normal distance $(\boldsymbol{c} - \tilde{\boldsymbol{c}}) \cdot \boldsymbol{n}$ from the object plane center $\boldsymbol{c}$ to the feature plane center $\tilde{\boldsymbol{c}}$. 2) Axis distance $\tilde{\boldsymbol{n}} \cdot \boldsymbol{k}_\star$ for each object plane axis $\boldsymbol{k}_1/\boldsymbol{k}_2$ and the feature plane normal $\tilde{\boldsymbol{n}}$.

The parameters (o, z_1, z_2), and thus the object plane's position and orientation are optimized during the adjustment in order to minimize the normal and axis distances between object plane and all corresponding feature planes (Fig. 7). The plane measurement equation is given by

$$\begin{aligned} 0 &= (\boldsymbol{c} - \tilde{\boldsymbol{c}}) \cdot \boldsymbol{n} &+ \epsilon_n, \\ 0 &= \tilde{\boldsymbol{n}} \cdot \boldsymbol{k_1} &+ \epsilon_{k1}, \\ \underbrace{0 = \tilde{\boldsymbol{n}} \cdot \boldsymbol{k_2}}_{\text{constraint}} &&+ \underbrace{\epsilon_{k2}}_{\text{error}}. \end{aligned} \tag{5}$$

Strictly speaking, this is not an explicit measurement, but rather a constraint. Note that the above equations implicitly depend on the platform trajectory and scanner calibration as in Equation (3). At this point, all errors occurring in the above measurement models are assumed Gaussian, uncorrelated and therefore independent. The relevant standard deviations for the Gaussian noise of the inertial measurements are determined in a static calibration. For the LiDAR correspondences, they are derived from the PCA results, taking into account LiDAR angular and ranging accuracy. The GNSS error standard deviations are internal estimates provided by the GNSS processing solution. However as argued above, the GNSS positions are not uncorrelated. Therefore, we now introduce a stochastic model for the time-correlated error component.

2.2 Stochastic Error Model for Loosely Coupled GNSS Integration

Assuming that the GNSS position measurements include not only white noise but also a time-correlated error term, the measurement equation can be extended to

$$\tilde{\boldsymbol{p}} = \boldsymbol{p}(t, \boldsymbol{x}_o) + \mathbf{R}(t, \boldsymbol{x}_o)\boldsymbol{l}_a + \underbrace{\boldsymbol{\nu}}_{\substack{\text{time-}\\ \text{correlated}\\ \text{errors}}} + \underbrace{\boldsymbol{\varepsilon}}_{\substack{\text{uncorrelated}\\ \text{errors}\\ =\\ \text{measurement}\\ \text{noise}}}. \tag{6}$$

A simple, yet effective way of modelling time-correlated errors is a first-order Gauss-Markov (FOGM) process, defined recursively by

$$\nu_i = \underbrace{\exp\left(-\frac{t_i - t_{i-1}}{T}\right)}_{=:a} \nu_{i-1} + w_i, \qquad w_i \sim N(0, \sigma_w^2). \tag{7}$$

This is an order 1 autoregressive process, where the autoregressive coefficient a is constrained by $0 < a < 1$. When the first sample ν_0 is also normally distributed with $\nu_0 \sim N(0, \frac{\sigma_w^2}{1-a^2})$, the process is stationary with covariance $\mathbb{V}(\nu_i) = \frac{\sigma_w^2}{1-a^2}$ and zero mean $\mathbb{E}(\nu_i) = 0$.

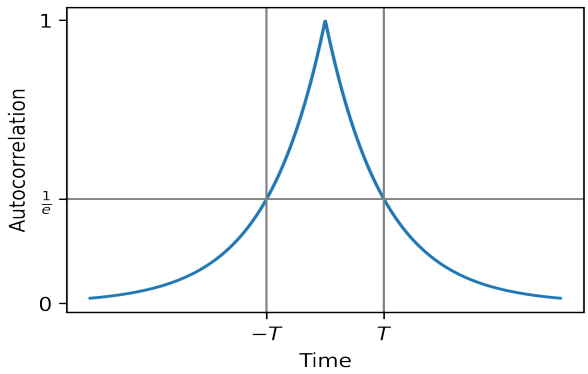

Fig. 8: Autocorrelation of first-order Gauss-Markov process ν

For each coordinate system axis of the local coordinate system, we model a separate Gauss Markov process. Each process is defined by two parameters, its process noise standard deviation and its correlation time. The process noise variance σ_w^2 controls the amount of stochastic noise added in each time step. While the measurement noise is uncorrelated, each v_i is a weighted sum of the past process noise realizations and therefore correlated in time. The correlation time T is a measure of how long it takes the process to become uncorrelated with itself; specifically, T refers to when the autocorrelation drops below $1/e$. If $T \to 0$, the additive white-noise error model is recovered, while for $T \to \infty$ the FOGM turns into a random walk. For errors in GNSS positioning, time correlation of around 10-30 seconds may be expected (from own experiments), but this can go up to several 100 seconds in the presence of multi-path effects (HAN & RIZOS 2000). Since in most instances, the applicable parameters of the Gauss-Markov process are not known, we propose to adapt the Cochrane-Orcutt estimator (COCHRANE & ORCUTT 1949) from linear least-squares with time-correlated errors to our specific non-linear least squares setting.

In our model, the unknown time-correlation applies only to the GNSS errors. The time-correlated component $\boldsymbol{v}$ is explicitly modelled by the parameters $\boldsymbol{b}_g$, assumed to follow a first-order Gauss-Markov process. The Cochrane-Orcutt estimator is adapted in the following way:

1. Estimate model parameters with uncorrelated GNSS measurement model.
2. Obtain an estimate of the process correlation time T and standard deviation σ by fitting a first-order Gauss Markov process to the residuals

$$\boldsymbol{r} := \tilde{\boldsymbol{p}} - \boldsymbol{p}(t, \boldsymbol{x}_o) + \boldsymbol{R}(t, \boldsymbol{x}_o)\boldsymbol{l}_a = \boldsymbol{v} + \boldsymbol{\varepsilon}. \tag{8}$$

   Per assumption, this is an FOGM process with additive measurement noise. For observation i, the process model has the form

$$\underbrace{\begin{pmatrix} r_x \\ r_y \\ r_z \end{pmatrix}_i}_{\text{GNSS residuals}} = \underbrace{\begin{pmatrix} v_x \\ v_y \\ v_z \end{pmatrix}_i}_{\text{Gauss-Markov process}} + \underbrace{\begin{pmatrix} \varepsilon_x \\ \varepsilon_y \\ \varepsilon_z \end{pmatrix}_i}_{\text{measurement noise}},$$
$$\begin{pmatrix} v_x \\ v_y \\ v_z \end{pmatrix}_i = \begin{pmatrix} a_x & 0 & 0 \\ 0 & a_y & 0 \\ 0 & 0 & a_z \end{pmatrix} \begin{pmatrix} v_x \\ v_y \\ v_z \end{pmatrix}_{i-1} + \underbrace{\begin{pmatrix} w_x \\ w_y \\ w_z \end{pmatrix}_i}_{\text{process noise}}. \tag{9}$$

   The coefficients (a_x, a_y, a_z) and hence the correlation times, as well as process noise variances and measurement noise variances can be estimated using standard state-space methods from time-series analysis (DURBIN & KOOPMAN 2012).
3. Estimate model parameters with time-correlated GNSS errors via non-linear least-squares.

Note that in the above, the measurement noise is assumed Gaussian, independent and identically distributed with no cross-correlation between the axes. This is not typically the case for the covariance matrices of the GNSS position measurements which are provided by the GNSS processing solution, as these include some correlations between the x-, y- and z-axis. This assumption is a limitation due to the implementation of the time-series estimation; the full covariance matrix of the GNSS position measurement is used in the actual adjustment.

3 Airborne Laser Scanning Case Study

3.1 Equipment and Dataset

The data for this case study was acquired with a RIEGL VUX-160[23] and an AP+50 GNSS/INS navigation system mounted on a Cessna 206 over Retz, a small town in Lower Austria. The flight trajectory is shown in Fig. 10. The flying altitude was 550 m above ground level with a ground speed of 57 m/s and a pulse repetition rate of 600 kHz, resulting in a point density per strip of 7 points per square meter.

The RIEGL VUX-160[23] is an airborne laser scanner with a mass of 2.65 kg, a field of view of 100 degrees, a scan speed of up to 400 lines/sec and a pulse repetition rate of up to 2.4 MHz. It is designed for corridor mapping applications with high point density. The instrument is based on time-of flight measurements at 10 mm accuracy, 5 mm precision, and a measurement range of up to 1800 m. It is able to capture up to 32 targets per pulse and thus offers excellent multi-target capabilities, which is especially important for power line surveying and forestry. The RIEGL VUX-160[23] offers a sophisticated scan pattern consisting of scan lines with periodically changing directions (Fig. 3). The scan directions in the center of the scan lines change consecutively from strictly nadir, to +10 degrees forward, and to -10 degrees backward. This scan pattern provides an almost complete 3D data set, as also vertical surfaces like the facades of buildings and objects (e.g. towers, masts, and poles) are accurately sampled by laser range measurements (Fig. 9). In addition, the nadir direction enables reliable data acquisition down to the bottom of narrow canyons.

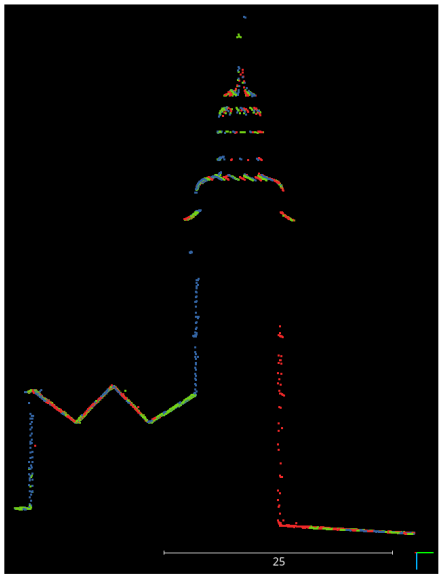

Fig. 9: Retz chapel. The points are colorized according to the three different view directions indicated in Fig. 4

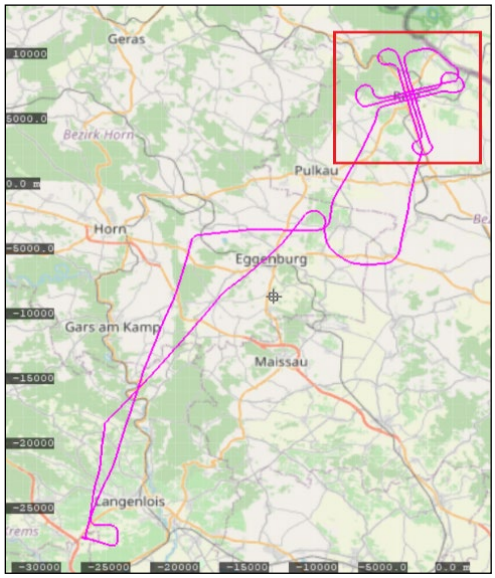

Fig. 10: Flight trajectory with 2×3 flight strips in a cross pattern

3.2 Results and Comparison

For comparison and to motivate the methodology, we compute a separate strip adjustment solution with the OPALS software (PFEIFER et al. 2014), using the approach developed by GLIRA et al.

2016. In this adjustment, laser scanner calibration (lever arm and boresight angles) are estimated as part of the adjustment, and the initial trajectory from GNSS/INS is corrected by estimating a constant offset in position and orientation per strip. Correspondences in the laser point cloud are established iteratively via a closest point algorithm, while the underlying GNSS and INS measurements are not considered.

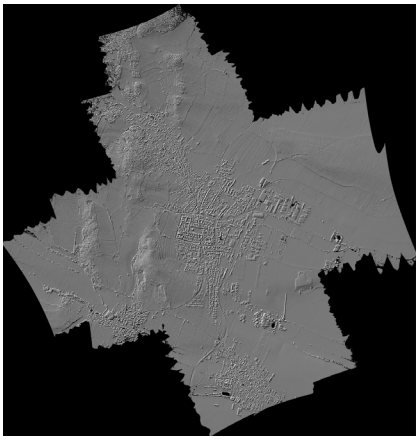

Fig. 11: DSM of all strips and views

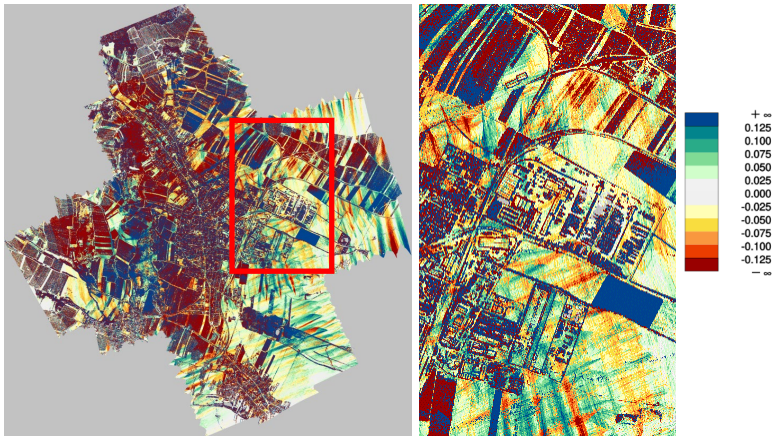

Fig. 12: Signed maximum strip difference of all strips

The study area contains a large number of fields and other vegetation, which will show up as large discrepancies in the strip differences (Fig. 12) due to differing viewing directions. For a clearer presentation, we will focus on the area marked in red. The strip differences show systematic errors up to 15 cm, presumably stemming in a large part from an inaccurate trajectory. These errors are on a timescale of a few seconds or less, making them impossible to correct with a constant per-strip offset. One approach would now be to allow not only an offset, but rather a time-varying correction using splines. This then leads to the problem of choosing the number of spline parameters or equivalently, the spacing of the spline knots: If the spacing is too large, the errors will not be fully correctable. A smaller spacing however may quickly lead to overfitting and deformation of the trajectory and in consequence the point cloud. This leads us to the approach detailed above: Keep the measurements from GNSS and INS and integrate them with LiDAR correspondences.

The GNSS/INS/LiDAR-integration is carried out as described in Section 2. Inertial measurements are available with 200 Hz, GNSS positions with 1 Hz. The frequency and number of the LiDAR plane correspondences depends on the rasterization parameters. Here, a cell size of 2.5 m was used, followed by a 4x sub-sampling of all planes and a 24x sub-sampling of all horizontal planes. The forward/nadir/backward viewing angles allow extraction of correspondences even on short timescales (within a strip) and with very steep slopes (e.g., facades). Comparing Fig. 13 and Fig. 14 there are two major differences: The overall number of extracted objects is much lower with only the nadir view, because in-strip overlaps of the different views are not considered. However, in addition to an overall reduction in the number of extracted object planes, there are almost no vertical planes left at all, as these are rarely seen with a nadir viewing angle.

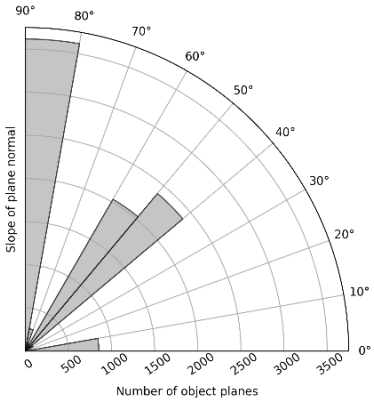

Fig. 13: Number of extracted object planes per 10-degree interval of the slope of the plane normal, for all views of all strips

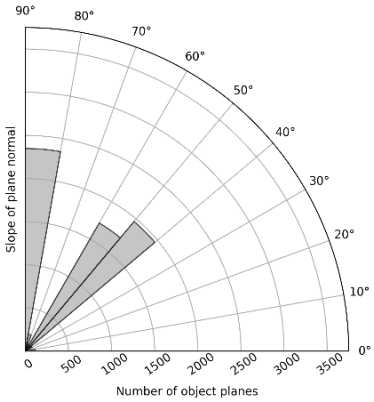

Fig. 14: Number of extracted object planes per 10-degree interval of the slope of the plane normal, for the nadir view of all strips

Analogously to Fig. 12, the strip differences after the batch least-squares adjustment using GNSS positions, inertial measurements and LiDAR plane correspondences are shown in Figure 15. However, the errors have different characteristics compared to those in Fig. 12: There are large-scale differences of up to 15 cm, while the smaller-scale difference patterns have mostly disappeared. While it is hard to pinpoint the error source exactly due to the complexity of the model, discrepancies that are constant over wider areas point towards an inaccurate platform position. As shown in Fig. 17, the residuals for the GNSS position observations increase drastically within all strips. In order to achieve a consistent point cloud, the modelled antenna position has to diverge significantly from the measured GNSS position.

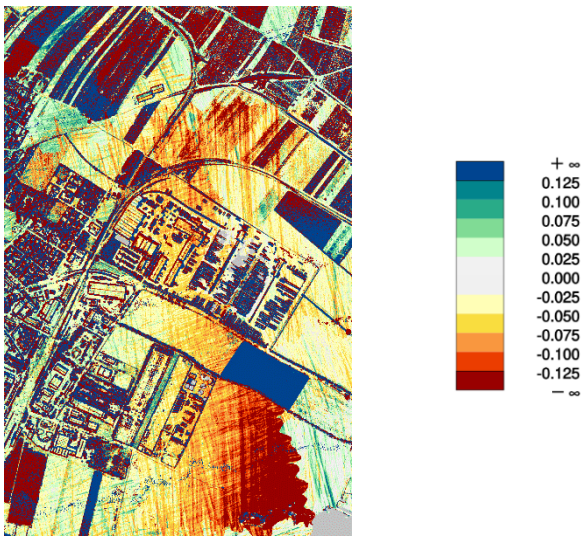

Fig. 15: Strip differences of GNSS/INS/LiDAR-adjustment with uncorrelated GNSS positions

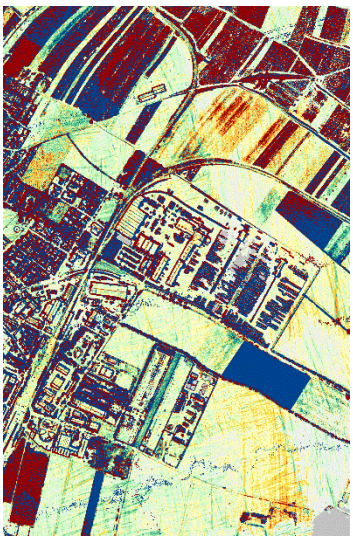

Fig. 16: Strip differences after GNSS/INS/LiDAR-adjustment with time-correlated GNSS position errors.

The differences between the GNSS position measurements and the modelled antenna position (Fig. 17) have a systematic time-dependence. This is contrary to the stochastic assumption of measurements with independent zero-mean noise, resulting in the strip differences seen above. The discrepancies between the model and the GNSS measurements are largest in the center of each strip, where LiDAR correspondences with the cross-track strips are present.

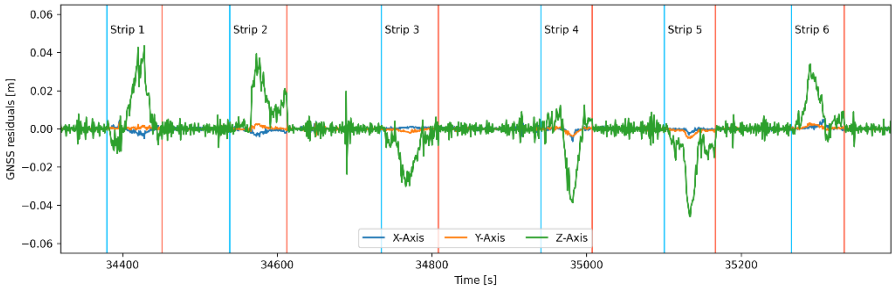

Fig. 17: GNSS residuals without time-correlated error model

Table 2 shows the estimated correlation time and process noise standard deviations of the GNSS position residuals. The correlation time is 20-35 seconds depending on the axis. The process noise standard deviation is 10x higher for the z-axis than for the x- and y-axis. This partially due to the LiDAR measurements, as the majority of the correspondences are horizontal planes, which constrain the trajectory only in the height component. The increased process noise standard deviation in the z-axis may also suggest the actual error process is more complicated than the modelled FOGM process. Nevertheless, for representing the time-correlated characteristics of the residuals in Fig. 17, the FOGM model is a substantial improvement compared to assuming independent measurements.

Tab. 2: Estimated Gauss-Markov process parameters

	x-Axis	y-Axis	z-Axis
Correlation time T [s]	21.14531	26.97508	34.87152
Process noise standard deviation[1] σ_w [m]	0.00021	0.00019	0.00227

With the estimated process parameters, we can now model the time-correlated GNSS bias within the least-squares adjustment, while all other parameters remain the same. The resulting point cloud shows drastically reduced differences compared to before (Fig. 16). Judging from the comparatively homogenous strip differences of the rooftops on the lower left side of Fig. 16, there seems to be no significant lateral error. The magnitude of the estimated bias $\boldsymbol{b}_g$ is around 4-5cm for the z-axis, and the GNSS residuals now show no obvious time-correlation (Fig. 18). Some discrepancies between different strips and between views within a strip do remain, the cause of which will be investigated in future work.

[1] The noise standard deviations are of course only applicable for our time sampling frequency of 1Hz (or equivalently, a time step size of 1s) and would have to be converted for other sampling frequencies.

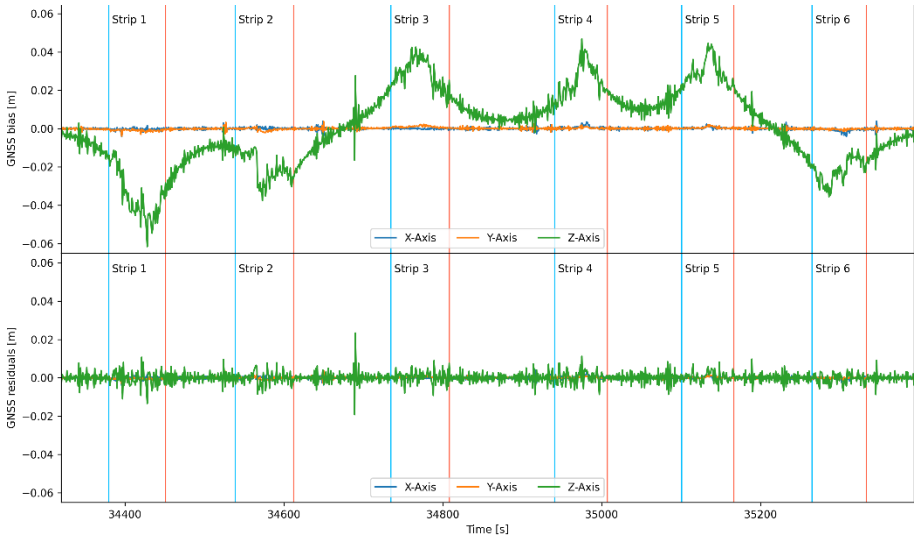

Fig. 18: GNSS errors and residuals with time-correlated error model

4 Conclusion

In this contribution, we presented a method for integrating GNSS, INS and LiDAR data, which takes into account the time-correlation of the GNSS position measurements. The approach was validated with an ALS dataset where it achieved reduced strip differences compared to a classic strip adjustment approach using a constant per-strip trajectory correction and to the GNSS/INS/LiDAR-integrated adjustment without explicit modelling of the GNSS errors' time-correlation. However, this does not conclusively disprove the existence of strip deformations, which might occur with a more flexible spline-based strip adjustment. In future work, it would be prudent to perform a systematic comparison of the results not only in terms of internal consistency (i.e., strip differences), but also with accurate reference data in order to rule out these systematic deformations in the point cloud.

5 Bibliography

AGARWAL, S., MIERLE, K. & The Ceres Solver Team, 2022: Ceres Solver, https://github.com/ceres-solver/ceres-solver.

COCHRANE, D. & ORCUTT, G.H., 1949: Application of Least Squares Regression to Relationships Containing Auto-Correlated Error Terms. Journal of the American Statistical Association, **44**(245), 32-61.

DURBIN, J. & KOOPMAN, S.J., 2012: Time Series Analysis by State Space Methods. 2nd ed., Oxford University Press, Oxford.

FARRELL, J.A., SILVA, F.O., RAHMAN, F. & WENDEL, J., 2022: Inertial Measurement Unit Error Modeling Tutorial: Inertial Navigation System State Estimation with Real-Time Sensor Calibration. IEEE Control Systems Magazine, **42**(6), 40-66.

FILIN, S. & VOSSELMAN, G., 2004: Adjustment of Airborne Laser Altimetry Strips. Int. Arch. Photogramm. Remote Sens. Spatial Inf. Sci., 258-263.

GLIRA, P., PFEIFER, N. & MANDLBURGER, G., 2016: Rigorous Strip Adjustment of UAV-based Laserscanning Data Including Time-Dependent Correction of Trajectory Errors. Photogrammetric Engineering & Remote Sensing, **82**(12), 945-954.

GROVES, P.D., 2013: Principles of GNSS, Inertial, and Multisensor Integrated Navigation Systems. 2nd ed., Artech House, Boston.

HAN, S. & RIZOS, C., 2000: GPS Multipath Mitigation Using FIR Filters. Survey Review, **35**(277), 487-498.

KAGER, H., 2004: Discrepancies Between Overlapping Laser Scanner Strips-Simultaneous Fitting of Aerial Laser Scanner Strips. Int. Arch. Photogramm. Remote Sens. Spatial Inf. Sci., **35**, 555-560.

KIM, M.-J., KIM, M.-S. & SHIN, S.Y., 1995: A General Construction Scheme for Unit Quaternion Curves with Simple High Order Derivatives. Proceedings of the 22nd Annual Conference on Computer Graphics and Interactive Techniques - SIGGRAPH '95, ACM Press, 369-376.

NIU, X., WU, J. & ZHANG, Q., 2018: Research on Measurement Error Model of GNSS/INS Integration Based on Consistency Analysis. Gyroscopy and Navigation, **9**(4), 243-254.

PFEIFER, N., MANDLBURGER, G., OTEPKA, J. & KAREL, W., 2014: OPALS – A Framework for Airborne Laser Scanning Data Analysis. Computers, Environment and Urban Systems, **45**, 125-136.

PÖPPL, F., NEUNER, H., MANDLBURGER, G. & PFEIFER, N., 2023: Integrated Trajectory Estimation for 3D Kinematic Mapping with GNSS, INS and Imaging Sensors: A Framework and Review. ISPRS Journal of Photogrammetry and Remote Sensing, **196**, 287-305.

TAKASU, T. & YASUDA, A., 2009: Development of the Low-Cost RTK-GPS Receiver with an Open Source Program Package RTKLIB. International Symposium on GPS/GNSS, Jeju, Korea, **7**.